A new actin depolymerase: a catch bond Myosin 1 motor

Julien Pernier[1,2,3]+, Remy Kusters[1,2,4]+, Hugo Bousquet[2,3], Thibaut Lagny[1,2,3], Antoine Morchain[1,2], Jean-François Joanny[1,2,5], Patricia Bassereau[1,2]*, Evelyne Coudrier[2,3]*

1. Laboratoire Physico Chimie Curie, Institut Curie, PSL Research University, CNRS UMR168, 75005 Paris, France
2. Sorbonne Universités, UPMC University Paris 06, 75005 Paris, France
3. Institut Curie, PSL Research University and C.N.R.S. UMR 144, 26 rue d'Ulm, Paris, France
4. University Paris Descartes, Center for Research and Interdisicplinarity (CRI), 8 Rue Charles V, Paris, France
5. ESPCI Paris, PSL Research University, 10 rue Vauquelin 75005 Paris, France

+ : equally contributing authors
*: corresponding authors: patricia.bassereau@curie.fr and evelyne.coudrier@curie.fr

Abstract

The regulation of actin dynamics is essential for various cellular processes. Former evidence suggests a correlation between the function of non-conventional myosin motors and actin dynamics. We investigate the contribution of the catch-bond myosin1b to actin dynamics using sliding motility assays. We observe that sliding on myosin1b immobilized or bound to a fluid bilayer enhances actin depolymerization at the barbed end, while sliding on the weak catch-bond myosin II has no effect. Our theoretical model shows the pivotal impact of the catch-bond behavior of a motor on depolymerization of sliding actin filaments. The catch-bond prolongs the attachment time of the motor at the barbed end due to the friction force exerted by the sliding filament; thereby this motor exerts a sufficient force on this end to promote depolymerization. This work reveals a non-conventional myosin motor as a new type of depolymerase.

Actin filaments (F-actin) form a variety of dynamical architectures that govern cell morphology and cell movements. The dynamics of the actin networks are regulated in space and time by the assembly and disassembly of actin polymers under the control of regulatory proteins. Cortical actin organizes lateral movement of transmembrane proteins and participates in membrane signaling by interacting transiently with the plasma membrane [1]. One class of actin-associated molecular motors, the single-headed myosin 1 proteins, bridges cortical actin to the plasma membrane. Polymerization of actin filaments at the plasma membrane generates forces on the membrane as well as on their membrane linkers. Inversely myosin 1 can exert and sustain pN forces on F-actin [2].

This important class of myosins contains a motor domain at its N-terminus that binds F-actin in response to ATP hydrolysis, a light chain binding domain (LCBD) that binds calmodulin (in most cases), and a Tail domain at the C-terminus (Fig. 1A) [3]. The Tail domain encompasses a tail homology domain (TH1) with a pleckstrin homology motif (PH) that binds phosphoinositides (Fig. 1A). Beside the involvement of myosin 1 proteins in a large variety of cellular processes including cell migration and membrane trafficking [3], manipulation of Myosin 1 expression has revealed a correlation between these myosins and actin network architecture [4, 5, 6, 7]. In particular, under- or overexpression of one of these myosins, myosin 1b (Myo1b), affects the organization of the actin cytoskeleton in the juxtanuclear region of HeLa cells [4] and in growth cones of cortical neurons [6]. However, the role of these motors in actin dynamics remains to be explored.

Given that Myo1b is mechanosensitive and is a catch bound motor (the time Myo1b remains bound to F-actin strongly increases with an applied load), Myo1b could in turn exert a force on polymerizing actin filaments [8, 9]. When bound to a substrate and in contact with F-actin, Myo1b has different configurations over time as a function of the ATP hydrolysis stage. When attached, Myo1b performs a first power-stroke and propels the actin filament over a distance d_1 towards the minus-end (being a plus-end motor) and depending on the applied force, it performs a second power stroke d_2. Due to its catch-bond behavior, it thus remains attached to the filament for a time that depends on the applied force F. It eventually detaches independently of the force but depending on the ATP concentration with a rate $\varpi_{det}(C_{ATP})$ [9] (Fig. 1B). Increasing the ATP concentration hence increases the detachment rate, which in turn could impact the growth of actin filaments. In this paper, we use *in vitro* F-actin gliding assays (Fig. 1C) and total internal reflection fluorescence (TIRF) microscopy to study the effect of Myo1b on actin polymerization dynamics, with the motors either immobilized on a solid substrate (Fig. 1C, III) or bound to a fluid supported bilayer, which mimics cell membranes (Fig. 1C, IV).

The sliding velocity v_f of single stabilized F-actin on Myo1b immobilized on a glass coverslip (Fig. S1A, top and Movie S1) and the sliding velocity v_f and the polymerisation rate v_p of single polymerizing F-actin (Fig. S1A, bottom and Movie S1) (Materials and Methods), both in the presence of 0.3% methylcellulose for keeping the filaments in the TIRF field, were measured by image analysis. At high Myo1b density (8000 μm^{-2}) (for the motor density measurement, see Materials and Methods and Fig. S1B), both stabilized and polymerizing filaments move with the same average sliding velocity $v_f = 56.4 \pm 15.4$ nm.s^{-1} and $v_f = 53.9 \pm 5.5$ nm.s^{-1}, respectively (Fig. 2A, Fig.2B, Movie S2 and Table S1) in the presence of 2 mM ATP (above saturation for motor activity) [10]. In both cases, this velocity decreases by about a factor two when decreasing the Myo1b density by a factor of twenty (Fig. S2B, S2C, Table S1) or when reducing the ATP level to 0.2 mM (Fig. 2A,B, Movies S2, S3) below saturation for Myo1b, but not affecting actin polymerization (Table S2).

To describe the actin filament sliding on Myo1b taking into account the force and ATP dependence, we extend the two state cross-bridge model [11] to a three-state cross-bridge model in order to explicitly include the two distinct substeps observed by Laksoo et al. [9]; (Fig. 1B,

Material and Methods). Increasing the ATP concentration increases the filament sliding velocity v_f, while the fraction of motors in the ATP-dependent state 2 decreases; however it lowers the catch-bond dependent transition rate, $\omega_{1\text{-}2}$ (Fig. 1B). This in turn increases the time that the catch-bond motor spends in state 1, in contrast with a weakly catch-bond motor such as myosin II (MyoII) (Fig. S3E). By matching the force-dependent transition rate ($\omega_{1\text{-}2}$) and the ATP dependent detachment rate (ω_{det}) we calculate the stationary sliding velocity of the filament, at the two measured ATP concentrations ($v_f \approx 55\,nm/s$ at $C_{ATP} = 2mM$ to $v_f \approx 25\,nm/s$ at $C_{ATP} = 0.2mM$, Fig. S3F) for Myo1b as well as for MyoII ($v_f \approx 255\,nm/s$ at $C_{ATP} = 2mM$). This model describes accurately the effect of the catch-bond on the sliding velocity (Fig. S3F).

We next investigated the impact of Myo1b on actin polymerization upon filament sliding. The actin assembly-disassembly kinetics are an order of magnitude faster at the barbed (plus) end than at the pointed (minus) end [12]. Thus, we measured the elongation ΔL of F-actin at the barbed-end versus time (Fig. 2C). Strikingly, filament sliding on Myo1b decreases the actin polymerization rate v_p, as compared to actin polymerization in the absence of Myo1b (Fig. 2D and Movie S3). This effect is stronger for high filament sliding velocity (in the presence of 2 mM ATP) and weaker at lower Myo1b density on the substrate (Fig. S2B, Fig. S2D, Movie S3 and Table S2). We also measured the dynamics of the pointed (minus) end by detecting the relative movement of this extremity compared to a fiducial point on the filament. In contrast with the barbed end, we did not observe any filament length variation (Fig. S2A and Movie S4), thus filament sliding on the motors reduces the actin polymerization rate at the barbed-end only. As a control, we tested the impact on actin polymerization of free Myo1b present only in the bulk, or immobilized on the surface but inactivated (Fig. S2B,D and Movie S5); we did not observe any effect on polymerization (Fig. S2E). Moreover, although actin filaments slide five-fold faster on non- or weak catch-bond myosins such as muscle myosin II (MyoII) [13], at the same bulk monomeric-actin (G-actin) concentration (Fig. 2A,B and Movie S6), the actin polymerization rate remains similar to the control (Fig. 2C, D). These observations demonstrate that an immobilized myosin motor with intact activity and a catch-bond behavior reduces the actin polymerization rate at the barbed-end up to a factor two (Table S2), in contrast to a weak catch-bound myosin such as muscle MyoII.

Dynamics at the barbed-end results from a balance between the rate of association of G-actin k_{on} and the rate of dissociation k_{off}; steady state is obtained at the critical concentration C_{c^+}. Classically, these dynamical parameters are deduced from the measurement of the variation of the polymerization rate v_p with G-actin concentration C_m: $v_p = k_{on}C_m - k_{off}$. By varying the G-actin bulk concentration from 0.1 to 1 µM in the presence of either 0.2 mM and 2 mM ATP, we observed that the slope corresponding to k_{on} is unchanged when F-actin slides over Myo1b, whereas C_{c^+} which is the ratio between k_{off} and k_{on} increases (Fig. 2D) demonstrating that k_{off} increases under these conditions (Fig. 2D and Table S2). Still, in the absence of G-actin in the bulk, filaments depolymerize faster when they slide over Myo1b (Fig. S2F, G and Movie S7). Interestingly, the dissociation rate is weakly affected when reducing Myo1b density (Fig. S2E and Table S2). The decrease of the dissociation rate is due to a lower sliding velocity of the filament. As expected, the sliding velocity of the filament decreases weakly with the motor density. In our model, this effect is associated with the impact of the external hydrodynamic drag on the filament, which eventually slows down the motors. In contrast, while sliding on MyoII is much faster, this myosin has no influence on k_{off} at the barbed-end of the filament (Fig. 2D and Table S2). Together, these observations indicate that the catch-bond Myo1b is an actin depolymerase.

One possible mechanism for this depolymerase activity would be that Myo1b induces actin depolymerisation by modulating the torsion of the filaments [14]. In this case, the polymerization kinetics would be expected to depend on the filament length with a twist gradient inversely proportional to the length. However this is not what we observe (Fig. S2H), excluding an explicit role of filament torsion due to motor attachment along the filament.

We thus developed a theoretical model for actin polymerization when filaments slide on motors depending on their catch-bond properties (Fig. 1B, Fig. 2E, and Materials and Methods). Due to the catch-bond behavior of Myo1b, the transition rate between states 1 and 2 in Fig. 1B) decreases with increasing filament sliding velocity. Thus, the motors remain in state 1 for an increased time, inducing a larger friction on the sliding filaments as compared to non-catch-bond motors such as MyoII. We assume that this friction between the motor and the filament generated along the filament increases the attachment time of the single molecular motor at the barbed end and thus this motor induces a force at this extremity sufficient to promote depolymerization. We have quantified this effect by assessing the impact of this force on the increase of the actin dissociation rate. For this we have introduced an exponential decay of the dissociation rate with the force on the filament over a characteristic force f^* [15] (Materials and Methods Eq. SE10). This characteristic force quantifies the force sensitivity of the depolymerization rate of actin k_{off}. Using our model we have determined $f^* \approx 5 - 6pN$ (Fig. S5A). $f^* \gg 6pN$ would make the actin filament insensitive to forces applied by the motor (Fig. S5A). $f^* \ll 6pN$ would impact the dissociation at low ATP concentration, precluding the stability of the filaments in the presence of motors (Fig. S5A). This model shows that the catch-bond behavior of Myo1b drastically increases the F-actin depolymerization at the barbed-end while a weakly-catch bond MyoII motor barely impacted F-actin depolymerization in agreement with our experiments.

In cells, Myo1b is bound to the fluid plasma membrane lipid bilayer through the interaction of its PH domain with PI(4,5)P2 [16], and thus it is not immobilized (Fig. 3A). We mimic experimentally these cellular conditions by analyzing the impact of Myo1b on actin dynamics when bound to a glass-supported lipid bilayer (SLB) composed of 79.5% POPC, 20% L-α-phosphatidylinositol-4,5-bisphosphate (PI(4,5)P2) and 0.5% Rhodamine-PE or Atto488-DOPE (mol/mol) (Fig. 1C and Fig. 3) (Materials and Methods). We checked using fluorescence recovery after photobleaching (FRAP) that membrane fluidity was preserved in the SLB with bound Myo1b (Fig. 3A and Fig. S6). The lipid diffusion coefficient was in agreement with data published on SLBs composed of pure POPC [17]. After recruitment on the SLB, Myo1b diffuses freely in the plane of the membrane (Fig. 3A). We did not observe any difference between experiments with or without methylcellulose in the bulk. In addition, the lipids continue to diffuse freely even when Myo1b diffusion is strongly decreased by a dense actin network (Fig. 3A) due to an emerging coupling when a filament bridges multiples motors. The diffusion coefficients are close to those measured in cell membranes (Fig. 3A), showing that in our *in vitro* experiments, the fluidity of the membrane is preserved. As previously reported [18], myosin 1 proteins bound to a lipid bilayer exert a force strong enough to propel actin filaments in spite of the fluidity of the support. We confirmed that in the presence of 2 mM ATP and at a similar Myo1b density as when immobilized (8500 μm^{-2}), stabilized and polymerizing F-actin slides on Myo1b bound to SLBs, although with a velocity reduced by about 25%: v_f = 37.6 ± 7.3nm.s^{-1} and v_f = 39.3 ± 8.2nm.s^{-1} respectively (Fig. 3B, Fig. 3C, Movie S8 and Table S1).

We have calculated the relative contributions of the viscous drag of the bulk and of the lipid bilayer on the motion of the filaments. First, we have considered F-actin moving in water ($\eta_b = 10^{-3} Pa.s$) above Myo1b bound to a SLB (Fig. 3D). We estimate that, since the in-plane viscous drag between the motor and the lipid bilayer is much larger than the bulk

viscosity experienced by the actin filaments, the velocity of the filament-motor couple, v_m, practically vanishes. Thus, filaments slide with a velocity $\widetilde{v_f}$ similar to that measured for immobilized motors: $\widetilde{v_f} \approx v_f$ (Fig. S7). However, the presence of methylcellulose in the assay to maintain the F-actin in the vicinity of the bilayer increases the viscosity of the bulk (10^{-2} Pa.s at 0.3%, product information Sigma) as well as the crowding effects between nearby filaments. This reduces the effective sliding speed of the filament $\widetilde{v_f}$ since part of the sliding is dissipated by in-plane motion of the motors in the bilayer (Fig. S7). This can explain why in our experiments, F-actin moves over SLB-bound Myo1b but with a slightly reduced velocity as compared to immobilized Myo1b (Fig. 3C, Table S1). This is in line with the results by Grover et al [19] showing a decreased gliding velocity of membrane-anchored kinesins due to their slippage in the lipid bilayer.

In these experimental conditions, we observed a significant increase of the actin depolymerization rate at the barbed end k_{off} when filaments slide on Myo1b bound to a SLB, although weaker than for immobilized Myo1b, while keeping the polymerization rate unchanged (Fig. 3E, Fig. 3F and Table S2). We conclude that the dissipation of sliding filaments in SLBs is low enough to let Myo1b exert a significant dissociation force even when bound to a fluid membrane (See force balance in Fig. 3G).

As previously shown, MyoII induces actin network contraction, potentially leading to filament buckling and breaking [20, 21]. However, we show here that muscle MyoII which is a weak catch-bond [13] in the pN force range, does not affect actin polymerization dynamics. Different actin-binding proteins are already known for preventing actin polymerization (capping protein) [12], enhancing it (formin) [22, 23] or depolymerizing actin (ADF/cofilin) [24, 25] at the barbed end. Also, some kinesin motors, e.g., kinesins 8 and 13, have been shown to depolymerize microtubules [26, 27]. We show here for the first time that increasing the sliding speed of the actin filaments through increasing the ATP-concentration drastically impacts the of the actin dissociation rate k_{off} at the barbed-end only for catch-bond motors (Tables S1 and S2). Note that the catch-bond effect on the actin growth is due to the longer attachment time of the Myo1b motor, but other molecular mechanisms that increase the duty ratio would potentially lead to a similar effect on actin dissociation. Another Myosin 1 (Myosin 1c) that is also a catch-bond, might regulate actin dynamics at the barbed-end. Nevertheless, the lifetime of its attachment to actin under load is ten times lower than for Myo1b [28], thus we expect its impact on actin dynamics to be moderate as compared to Myo1b, but this remains to be tested.

Experimental evidence supports a role of several Myosin 1 proteins in membrane remodeling [3]. Similarly to capping proteins [29], Myo1b and perhaps other Myosin 1 proteins could shape membranes by regulating the growth of filaments at the plasma membrane. Alternatively, Myo1b could shape membranes by inducing stresses in the cortical actin. Indeed, Myo1b induces actin movement and reduces actin growth when bound to supported bilayers, as shown in our experiments. Since the fluidity of our synthetic membranes and of cellular membranes are similar (Fig. 3A), we propose that Myo1b has the same function in cells. Collectively, these motors could drive the sliding of actin filaments at the membrane surface, which could create stresses that relax by deforming the cortex and the attached membrane. Interestingly, when Myo1b is bound to a deformable giant liposome, we observed that it produces membrane invaginations in presence of stabilized actin filaments (Fig. S8).

Myo1b's influence on actin dynamics can control the organization of actin networks, as reported in growth cones [6]. An actin network can be impacted by Myo1b in different ways. It can reduce the length of actin filaments, as shown by this work, and thus change the mesh-size, or the cortical thickness and consequently the cortical contractibility [30]. Whether or not it can affect the Arp2/3-dependent branched actin network and/or formin-dependent actin bundles remains to be explored. Moreover, since Myo1b is specifically present at the interface

between the plasma membrane and the cortical actin, Myo1b may coordinate receptor signaling by arranging the cytoskeleton [31].

Besides myosin II and myosin 1 proteins, myosin VI has also been reported to influence the actin architecture during, e.g. spermatid individualization in Drosophila [32] or around melanosomes [33]. It might be time now to take a fresh look on the involvement of non-conventional myosins in actin dynamics and organization.

Materials and Methods

Protein purification

Actin was purified from rabbit muscle and isolated in monomeric form in G buffer (5 mM Tris-HCl, pH 7.8, 0.1 mM $CaCl_2$, 0.2 mM ATP, 1 mM DTT and 0.01% NaN_3). Actin was labeled with Alexa 594 succimidyl ester-NHS [34].

Myosin II was purified from rabbit muscle as previously described [35].

Expression and purification of Myosin 1b: FLAG-myo1b was expressed in HEK293-Flp-In cells cultured in Dulbecco's modified Eagle medium supplemented with 10% fetal bovine serum and 0.18 mg ml^{-1} hygromycine in a spinner flask at 37 °C under 5% CO_2, and collected by centrifugation (1,000 g, 10min, 4 °C) to obtain a 4–5 g of cell pellet. The pellet was lysed in FLAG Trap binding buffer (30 mM HEPES, pH 7.5, 100 mM KCl, 1 mM $MgCl_2$, 1mM EGTA, 1 mM ATP, 1 mM DTT, 0.1% protease inhibitor cocktail (PIC), 1% Triton X-100) for 30 min at 4 °C and centrifuged at 3,400 g for 10 min at 4 °C. The collected supernatant was then ultracentrifuged (250,000 g, 60 min, 4 °C). The solution between pellet and floating lipid layer was incubated with 150 µl of anti-FLAG beads for 2 h at 4 °C. The beads were collected by centrifugation (1,000 g, 5 min, 4 °C). After a washing step, FLAG-myo1b was then eluted by incubating with 0.24 mg ml^{-1} of 3X FLAG peptide in 300 µl elution buffer (binding buffer without Triton X-100 supplemented with 0.1% methylcellulose) for 3 h at 4 °C. After removal of the beads by centrifugation (1,000 g, 3 min, 4 °C), the protein solution was dialyzed against elution buffer overnight at 4 °C to remove the 3X FLAG peptide. Myo1b was fluorescently labeled using Alexa Fluor 488 5-SDP ester [36]. "Dead" Myo1b was removed by ultracentrifugation (90,000 rpm, 20 min, 4 °C) with 1 µM F-actin in presence of 2 mM ATP. In some rare cells batches, purified Myo1b did not exhibit motor activity and was used as an "inactivated" motor in our experiments.

Supported lipid bilayer (SLB) preparation

SLBs were formed by fusion of small unilamellar vesicles (SUVs) prepared as follows. Lipid mixtures containing 79.5 % POPC, 20 % L-α-phosphatidylinositol-4,5-bisphosphate ($PI(4,5)P_2$) and 0.5 % Rhodamine-PE or Atto488-DOPE (mol/mol) were mixed together in a glass vial, dried with N_2, placed in vacuum desiccator for 1 hour, then rehydrated with Fluo F buffer (5 mM Tris-HCl- pH 7.8, 100 mM KCl, 1 mM $MgCl_2$, 0.2 mM EGTA, 0.2 mM or 2 mM ATP, 10 mM DTT, 1 mM DABCO, 0.01% NaN_3) for 30 min at room temperature, to a final lipid concentration of 2 mg/mL. After rehydration, the glass vial was vortexed to detach the liposomes. SUVs were formed by sonication, aliquoted and stored at -20 °C. For SLB formation by fusion, $CaCl_2$ was added to a final concentration of 5 mM, with 50 µl of SUVs. The solution was incubated in the chamber for 20 min and washed 5 times with Fluo F buffer 0.1 % BSA. The quality of the SLB was checked by FRAP.

Giant unilamellar vesicle (GUV) preparation

Lipid compositions for GUVs were 79.7 % POPC, 20 % L-α-phosphatidylinositol-4,5-bisphosphate (PI(4,5)P_2) and 0.3 % Texas Red DHPE. GUVs were prepared by using polyvinyl alcohol (PVA) gel-assisted method in a 200 mM sucrose buffer at room temperature for 2 hour as described previously [37].

Myosin 1b surface density

We measured the protein surface density (number of proteins per unit area) on solid surfaces or on SLBs by using a previously established procedure [38, 39]. It is calculated from a labeled proteins/lipids calibration. We first measure the fluorescence of POPC SLBs containing predefined amounts of Atto488-DOPE fluorescent lipids (DOPE*) to establish the relationship between the density of DOPE* n_{DOPE*} and the corresponding fluorescence intensity $I_{DOPE*SLB}$ (Fig. S1Ba). Assuming an area per POPC of 0.68 nm^2, we derive the calibration coefficient A corresponding to the slope of this curve. Note that A depends on the illumination and recording settings of the microscope.

$$n_{DOPE*} = A \times I_{DOPE*SLB}$$

Since Myo1b is labeled with Alexa488 and not Atto488, we have to correct this value by the ratio of fluorescence of the two fluorescent dyes in bulk deduced from the slope of the titration curves $\frac{I_{Alexa488}}{I_{DOPE*}}$ (Fig. S1Bb and c). We then obtained the surface density of the protein deduced from the measurement of the Myo1b-Alexa488 intensity I_{Myo1b*} as:

$$n_{Myosin1B} = \frac{A}{\frac{I_{Alexa488}}{I_{DOPE*}} \times Z} \times I_{Myo1b*}$$

where Z is the degree of labeling for the protein of interest (Here, Z=1). In our experiments, the calibration factor $\frac{A}{\frac{I_{Alexa488}}{I_{DOPE*}} \times \mathrm{Z}}$ is equal to 0.278.

Single-filament TIRF microscopy assays

The kinetics of single filament assembly was monitored by TIRF microscopy (Eclipse Ti inverted microscope, 100X TIRF objectives, Quantem 512SC camera). The experiments were controlled using the Metamorph software. Coverslips and glass slides were sequentially cleaned by sonication with H_2O, ethanol, acetone for 10 min, then 1M KOH for 20 min and H_2O for 10 min. In the case of supported lipid bilayer, first the coverslips and glass slides were cleaned by sonication with Hellmanex III (Hellma Analytics) for 30 min. Flow chambers were assembled with a coverslip bound to a glass slide with two parallel double-stick tapes. The chamber was incubated with 100 nM anti-myo1b antibody in G buffer (5 mM Tris-HCl, pH 7.8, 0.1 mM $CaCl_2$, 0.2 mM ATP, 1 mM DTT and 0.01% NaN_3) for 10 min at room temperature. The chamber was rinsed three times with buffer G 0.1 % BSA and incubated 5 min at room temperature. Then the chamber was incubated with 300 nM Alexa488-labeled myo1b in Fluo F buffer (5 mM Tris-HCl, pH 7.8, 100 mM KCl, 1 mM $MgCl_2$, 0.2 mM EGTA, 0.2 mM or 2 mM ATP, 10 mM DTT, 1 mM DABCO, 0.01% NaN_3) for 10 min at room temperature. Assays were performed in Fluo F buffer, containing 0.2 or 2 mM constant ATP, supplemented with 0.3% methylcellulose (Sigma) and with G-actin (10 % Alexa594) or F-actin (stabilized with phalloidin-Alexa594) at indicated concentrations. To maintaining a constant concentration of ATP in this assay an ATP regenerating mix, including 2 mM ATP, 2 mM $MgCl_2$, 10 mM creatine phosphate and 3.5 U/mL creatine phosphokinase, which constantly re-phosphorylates ADP into ATP to maintain a constant concentration of free ATP, was added.

The sliding and elongation velocities of actin filaments were analyzed by using Kymo Tool Box plugin of Image J software (https://github.com/fabricecordelieres/IJ_KymoToolBox).

Only filaments longer than 20 pixels are analyzed. When filaments slide on myosins, only those moving directionally during the whole sequence are selected. On each image of a sequence, a segmented line is manually drawn over a single filament, which generates a 10 pixel wide band. The plugin flattens the curved filaments and generates a kymograph. The accuracy on the displacement and the length of the filaments is of the order of the pixel size (160 nm).We consider that each actin subunit contributes to 2.7 nm of the filament length.

FRAP methods

For diffusion measurements, Fluorescence Recovery After Photobleaching (FRAP) experiments were performed through a X100 or X60 oil immersion objective on an inverted spinning disk confocal microscope (Nikon eclipse Ti-E equipped with a Prime 95B™ Scientific CMOS camera, Photometrics) equipped with a FRAP unit. Recovery curves (average of 5 independent experiments, performed on different circular regions of the SLB using the same bleaching conditions) were normalized to the initial intensity and fitted with a single exponential function. We derive the $\tau_{1/2}$ time corresponding to the time at which the fluorescence signal has recovered 50% of its value before bleach. We calculated the diffusion coefficient using the Soumpasis equation [40]:

$D_r = 0.224\,\frac{r^2}{\tau_{1/2}}$, where r is the radius of the bleached region.

Theoretical model for filament sliding: Myosin1b as a catch bond motor

Myosin 1b motor:

Myo1b is identified as a molecular motor with a catch-bond detachment rate: it responds to small resisting loads by dramatically increasing its duty ratio [9]. Single molecule experiments have established that the motor cycle of Myo1b contains two distinctive steps. In state 1, the motor performs a first power stroke of size $d_1 = 5.1$ nm. From state 1, the motor transits to state 2. After the transition, the motor relaxes its stress [9] and it performs a second power stroke of size $d_2 = 3.3$nm. The transition rate between state 1 and state 2, $\omega_{1-2}(F)$ depends on the applied force on the motor, F, and shows a catch-bond behavior (See Fig. 1b),

$$\omega_{1-2}(F) = \omega_0 \exp\left(-Fb/(k_B T)\right) + \omega_i. \tag{SE1}$$

Here, ω_i is the force independent transition rate observed at large force, ω_0, the force-dependent transition rate at vanishing force, b, the distance quantifying the strain sensitivity of the motor and $k_B T$ the thermal energy. Eventually, the motor detaches from the filament with a rate that depends on ATP concentration, C_{ATP} at a rate $\omega_{det}(C_{ATP})$, and follows Michaelis-Menten kinetics,

$$\omega_{det}(C_{ATP}) = \omega_{sat} \frac{C_{ATP}}{C_{ATP} + C^*} \tag{SE2}$$

where ω_{sat} is the detachment rate at saturated ATP concentrations and C^* the characteristic value above which the rate ω_{det} saturates.

Three-state crossbridge model:

To describe the actin filament sliding over Myo1b motors and to include the force and ATP dependences of the motor cycle, we extend the classical cross-bridge model [11,41] by explicitly including the force-and ATP dependent sub-steps of the motor cycle as depicted in Fig.1b. This model is valid for a filament sliding at constant velocity v_f and in the limit of a large number of molecular motors propelling the filament.

An actin filament sliding at speed v_f is transiently attached to a motor in either of the states 1 or 2, discussed in the previous paragraph (See Fig. 1b). We assume here that the two powerstrokes are instantaneous. While the motor is in state 1, it exerts a force on the filament:

$$F_1 = k_{cb}(v_f \tau_1 - d_1), \tag{SE3}$$

where k_{cb} is the cross-bridge stiffness of the motor and τ_1 is the time since attachment to the filament (the "age" of the motor in state 1) and d_1 the amplitude of the powerstroke. Similarly, while the motor is in state 2, it exerts a force on the filament of magnitude,

$$F_2 = k_{cb}(v_f \tau_2 - d_2), \tag{SE4}$$

where τ_2 is now the age of the motor in state 2, i.e. the time since the transition to state 2. The fraction of attached motors along the filament, both in state 1, ρ_1, and in state 2, ρ_2, as function of their respective ages, τ_1 and τ_2, evolve according to the following kinetic equations

$$\partial_{\tau_1} \rho_1 = \omega_{1-2}(F)\rho_1 + \delta(\tau_1)\omega_{on} n_d, \tag{SE5}$$

where $\delta(\tau_1)$ is the Dirac delta function, ω_{on} is the attachment rate and n_d is the fraction of detached motors. Note that we assume that during the powerstroke, the motor does not detach, i.e., $\omega_{1-2}(\tau < d_1/v_f) = 0$. Equivalently, ρ_2 evolves as,

$$\partial_{\tau_2} \rho_2 = \omega_{det}(ATP)\rho_2 + \delta(\tau_2) \int_0^\infty \rho_1(\tau_1)\omega_{1-2}(F) d\tau_1. \tag{SE6}$$

Solving this set of equations requires the determination of the total fraction of detached motors, n_d , which is obtained by summing the two populations of attached motors,

$$(1 - n_d) = \int_0^\infty \rho_1(\tau_1)d\tau_1 + \int_0^\infty \rho_2(\tau_2)d\tau_2. \tag{SE7}$$

The time-averaged force exerted by a single molecular motor along the filament is the sum of the contributions of the motors in states 1 and 2,

$$F_{mot} = k_{cb}\left(\int_0^\infty (v_f\tau_1 - d_1)\rho_1(\tau_1)d\tau_1 + \int_0^\infty (v_f\tau_2 - d_2)\rho_2(\tau)d\tau_2\right). \tag{SE8}$$

In Fig. S3 A,B we plot the integrands of the two contributions as functions of the motor ages in the corresponding state for (a) $C_{ATP} = 0.2mM$ and (b) $C_{ATP} = 2mM$. We use here the kinetic and mechanical parameters given in Table I, (see next section for the choice of these parameters). This figure shows that, initially, when $\tau < d/v_f$ the motor exerts a positive (propelling) force due to the power stroke, while for $\tau > d/v_f$ the motor exerts an opposing frictional force.

Depending on the relative values of the kinetic parameters, we identify two regimes. In the limit $\omega_{1-2}(F) \gg \omega_{det}(C_{ATP})$, the ATP dependent detachment is the limiting step and the motor mainly resides in state 2 (See Fig. S3C). This typically corresponds to low ATP concentrations. When $\omega_{1-2}(F) \ll \omega_{det}(C_{ATP})$, the motor mainly resides in state 1 and the force dependent (catch-bond) transition between states 1 and 2 impacts the detachment : this can be seen through the long tail in the force exerted by motors in state 2 in Fig S3B. To emphasize the role of the motor kinetics we show in Fig. S3D that a larger attachment rate ω_{on} increases the fraction of motors attached to the filament and also the fraction of motors in the force dependent state 1, n_1. A larger value of ω_{on} increases the fraction of time that the motor resides in the force dependent state 1 and therefore the impact of the catch-bond on the filament sliding becomes more important..

To further illustrate the role of the catch bond on the motor cycle, we plot the fraction of motors in state 1 ,n_1, and state 2, n_2, and compare a catch-bond motor as described above with a slip-bond motor where the transition rate is force independent $\omega_{1-2} = \omega_i + \omega_0$. We indeed observe that upon increasing the ATP concentration the fraction of motors in state 1 remains constant for the slip-bond motor, in contrast to the catch-bond motor for which n_1 increases. The fraction of motors in state 2 naturally decreases upon increasing C_{ATP}. The increased fraction of motors in state 1 increases the friction between the filament and the motor, decreasing the sliding velocity, relative to the velocity for a slip-bond motor (See Fig. S3F).

Determination of the Myo1b transition of detachment rate:

In this section, we estimate the kinetic rates and mechanical parameters of the Myo1b motor at the ATP concentrations used in our experiments. The values reported for the (un)-binding kinetics in Laakso et al. [9] were obtained at significantly lower ATP concentrations ($C_{ATP} = 50\mu M$) than reported here ($C_{ATP} = 0.2 - 2\ mM$). Using these values would imply attachment times up to 10-100 seconds, which are not compatible with sliding speeds of the order of 50nm/s; indeed they would imply stretching the Myo1b motor up to microns. Moreover it is worth noting that the detachment rates reported in Laakso et al. [9] are the combined kinetic rates of the two sub-steps (state 1 - state 2) and (state 2 - detached). Therefore we use the measured sliding velocities at the two ATP concentrations of our experiments to determine ω_i, ω_0 and ω_{sat} (See SE1 and SE2). Given the measured speeds we consider that the transition and detachment rates cannot be larger that one second, since otherwise this would imply motor extension larger than 50nm.

To match ω_{sat}, ω_0 and ω_i, we calculate the difference of the predicted and measured sliding speed at $v_f(C_{ATP} =$ 0.2 mM): $v_f = 25$nm/s and $v_f(C_{ATP} = 2$ mM): $v_f = 55$nm/s,

$$\text{error} = (\mathrm{v_f(C_{ATP=0.2mM})} - 25\mathrm{nm/s})^2 + (\mathrm{v_f(C_{ATP=2mM})} - 55\mathrm{nm/s})^2. \tag{SE9}$$

By calculating an error map as a function of ω_i and ω_0 for a range of ω_{sat} values we found that $\omega_{sat} \approx 25s^{-1}$ provides optimal matches in sliding speed relative to our experiments (See Fig. S4A and S4B). In Fig. S4C and S4E we show the respective values of the matching error for $\omega_{sat} = 10$ s^{-1} and $\omega_{sat} = 40$ s^{-1} indicating much higher errors relative to the $\omega_{sat} \approx 25s^{-1}$ plot.

This analysis provides a band of possible values that match the sliding velocities at ATP concentrations of 0.2 and 2 mM. This band of matching values (Indicated in Red in Fig S4D) corresponds to weak ($\omega_0/\omega_i \approx 1$) and strong

catch-bonds ($\omega_0/\omega_i \gg 1$). The strength of the catch-bond is measured here by the ratio between ω_0 (which is the transition ratio at vanishing force) and ω_i (which is the transition rate at high force). For our further analysis we choose a value $\omega_0/\omega_i = 62$ comparable to that reported by Laakso et al. [9].

Symbol	Value	Description
ω_i	$2s^{-1}$ †	Detachment rate of state 1 at saturated force (SE1)
ω_0	$128s^{-1}$ †	Detachment rate of state 1 at vanishing force (SE1)
ω_{sat}	$25s^{-1}$ †	Detachment rate of state 2 at saturated ATP concentration (SE2)
ω_{on}	$100s^{-1}$ †	Attachment rate of state 1
C^*	1 mM	The characteristic value above which the ω_{det} saturates
b	12 nm ‡	Distance characterizing the strain sensitivity of the motor
k_{cb}	0.2 pN/nm +	Cross-bridge stiffness of the motor

TABLE I: Kinetic parameters. †: Obtained by fitting the measured filament sliding speed v_f, ‡ [9], + : note that this value was determined for Myosin 1c and does not vary widely between different motor species and that the exact numerical value does not change our results qualitatively, e.g. for Myosin II, [41].

Filament sliding enhances actin depolymerization:

We showed in the previous section that due to the catch-bond characteristic of Myo1b, the motor spends a larger time in catch-bond state 1. Here we hypothesise that the prolonged attachment time of the last Myo1b motor to the barbed end of the filament induces a transient stress, and enhances the depolymerization. Experimentally (Fig. 2D), we show that, while the polymerization rate remains unaltered for filaments sliding over Myo1b, the depolymerization rate of the actin filament increases. This effect can be described by the average force dependent depolymerization rate [15],

$$k_{off} = k^0_{off}(n_d + \int_0^{-d_1/v_f} \rho_1(\tau_1)d\tau_1 + \int_0^{-d_2/v_f} \rho_2(\tau_2)d\tau_2 + \int_{-d_1/v_f}^{\infty} \rho_1(\tau_1)\exp\frac{k_{cb}(v_f\tau_1 - d_1)}{f^*}d\tau_1 + \int_{-d_2/v_f}^{\infty} \rho_2(\tau_2)\exp\frac{k_{cb}(v_f\tau_2 - d_2)}{f^*}d\tau_2), \tag{SE10}$$

where k^0_{off} is the depolymerization rate in the absence of applied force and f^* is the characteristic scale for the force sensitivity of the depolymerization rate. Since in the experiment, the filaments slide over catch-bond motors, the effective opposing frictional force on the filament is increased, enhancing the force at the plus-end and hence the depolymerization. Using SE10 we estimate the predicted increase in depolymerization rate as a function of ATP concentration for various values of the characteristic force, f^* (Fig. S5A). Note also that, depending on f^* this depolymerization rate may diverge in our theoretical model. We find that for $\omega_{on} = 100$ s^{-1}, $f^* \approx 5-6$ pN matches best our experimentally observed depolymerization rates.

The value of the attachment rate ω_{on} (detached - state 1) is a parameter that does not impact the sliding velocity at vanishing external force $F_{mot} = 0$. However, it impacts the fraction of motors in state 1 and state 2 as depicted in Fig S3D. An increase of ω_{on} leads to a larger number of motor cycles per unit time and therefore to a larger total time that the motor spends in the catch-bond state ρ_1. It increases both the fractions of motors in states 1 and 2. However, particularly at high ATP concentration, it shifts the equilibrium fraction from a state, primarily dominated by the ATP dependent state 2, to a state dominated by the force dependent catch bond state 1 (See Fig. S3D). Choosing a value for ω_{on} in the range of $10 - 10^4$ does not qualitatively impact the results at the experimental ATP concentrations as we show in Fig. S5B.

Identifying that myoII is a weak catch bond motor, we model it with a single force-independent rate ($\omega_0 = \omega_i = 0$), a power-stroke $d = 5.0$ nm and a cross-bridge stiffness $k_{cb} = 0.4$ pN/nm [11]. In Fig. 2b we observe that at $C_{ATP} =$ 2.0mM, the sliding velocity is $v_f \approx 255$nm/s. We calculate ω_{sat} that matches this sliding velocity: $\omega_{sat} \approx 77$ s^{-1}. Using this value, we plot the effect of the motors on the depolymerization rate of actin as a function of ω_{on} and find a small enhancement of the depolymerization rate $< 10\%$ for $\omega_{on} = 1 - 10^4$ s^{-1}, in agreement with our experimental data.

Taken together our model shows two interesting features. First, since the filaments are sliding on catch-bond Myo1b motors, their sliding speed decreases while the effective friction exerted by the motors on the filament increases.

Second, increasing the sliding velocity by e.g. increasing the ATP concentration increases the time that the motor spends under tension; it increases therefore the total friction force experienced by the filament and hence enhances the depolymerization, until saturation of ATP is reached. This effect on the depolymerization rate does not exist for slip-bond motors since their attachment time is a monotonically decreasing function with the ATP concentration as shown in Fig S3E.

In order to explicitly account for the density of motors along the actin filament, we now derive the sliding velocity of the filament in the gliding assay from the balance between the motor driving force, F_{mot}, and the drag force on the filament due to its surrounding $NF_{mot} = \xi v_f$ (N is the total number of motors along the filament). Depending on the magnitude of the friction coefficient, ξ, a decrease of the number of motors along the filament slows down the filament sliding v_f. This rationalizes the decrease of sliding velocity observed upon lowering the density of motors in the gliding assay (Fig. S2C, Table S1). In addition, a decrease of the motor density along the filament lowers the enhancement of depolymerization since the motors spend less time in the catch-bond state 1 (Fig. S3E), in agreement with our measurements (See Table S2).

Filament sliding on a lipid bilayer:

In order to estimate how the motor force is transmitted to the filament when the molecular motors are immersed in a lipid bilayer, instead of being rigidly anchored to a solid surface, we write a simplified force balance between the viscous friction force of the motor/filament and the force exerted by the molecular motors nF_{mot} where $n = \rho\ell$ is the number of attached motors along the filament of length ℓ,

$$-\xi_f \hat{v}_f = nF_{mot} \tag{SE11}$$

$$-\xi_f \hat{v}_f = -n\xi_m v_m \tag{SE12}$$

where ξ_m is the in-plane friction coefficient of the motor complex in the lipid bilayer, v_m, the speed of a molecular motor, ξ_f, the friction coefficient between the filament and the surrounding solution and $\hat{v}_f$, the speed of the filament in the assay. The first equation is the force balance on the filament and the second equation is the force balance on the filament and motors complex. We use here a simplified expression for the motor force estimated in Eq. SE 8, i.e., [41],

$$F_{mot} = f_s \left(1 - \frac{v_m - \hat{v}_f}{v_0}\right), \tag{SE13}$$

where f_s is the stall force of one motor and v_0 the motor speed at vanishing external force ($f_s \approx O(1)$ pN and $v_0 \approx 50$nm/s as calculated before with the more detailed model). The friction between the filament and the solution can be estimated as $\xi_f \approx 2\pi\eta_b/(\log \ell/b_f) \approx O(10^{-8})$ Pa.s.m, where we use the bulk viscosity of water $\eta_b = O(10^{-3})$ Pa.s and as a cut-off lengthscale, the size of the filament $\ell = O(10^{-5})$ m . Note however that the effective bulk viscosity can be significantly larger since the filament slides close to a surface. The friction between the motor complex and the lipid membrane is $\xi_m \approx 4\pi\eta_m/\log(l_0/L) \approx O(10^{-9})$ Pa.s.m [42], where L is the size of the membrane and l_0 the size of a motor (we estimate the membrane viscosity as $\eta_m \approx O(10^{-10})$ Pa.s. [4] and $\log(L/l_0) \approx O(1)$). Solving equations SE 11 and SE 12 gives the following values for the velocity of the filament, $\hat{v}_f$, relative to the velocity at zero external force on a solid substrate, v_0,

$$\frac{\hat{v}_f}{v_0} = -\frac{n\xi_m}{\xi_f + n\xi_m + v_0\xi_f\xi_m/f_s}, \tag{SE14}$$

and for the velocity of the motor, v_m,

$$\frac{v_m}{v_0} = \frac{\xi_f}{\xi_f + n\xi_m + v_0\xi_f\xi_m/f_s}, \tag{SE15}$$

For realistic values of the friction coefficient of water and typical force values we obtain a filament speed which is very close to the filament speed on a solid substrate $\frac{\hat{v}_f}{v_0} \approx 1$, indicating that, since the in-plane membrane friction of the motor is larger than the filament friction with the fluid, the motors are effectively immobile. However, upon increasing the viscous friction between the filament and the bulk by one/two orders of magnitude, potentially due to inter-filament friction (at high filament density) or to the addition of methylcellulose, the sliding speed of the filament diminishes significantly (See Fig. S7). Also decreasing the density of motors along the filament impacts the sliding speed since the effective friction between membrane and motor is proportional to the density of motors.

References

1. Köster DV, Mayor S. Cortical actin and the plasma membrane: inextricably intertwined. *Curr. Opin. Cell Biol.* 2016, **38:** 81-89.

2. Pyrpassopoulos S, Arpag G, Feeser EA, Shuman H, Tuzel E, Ostap EM. Force Generation by Membrane-Associated Myosin-I. *Sci. Rep.* 2016, **6:** 25524.

3. McIntosh BB, Ostap EM. Myosin-I molecular motors at a glance. *J. Cell Sci.* 2016.

4. Almeida CG, Yamada A, Tenza D, Louvard D, Raposo G, Coudrier E. Myosin 1b promotes the formation of post-Golgi carriers by regulating actin assembly and membrane remodelling at the trans-Golgi network. *Nat. Cell Biol.* 2011, **13:** 779-789.

5. Gupta P, Gauthier NC, Cheng-Han Y, Zuanning Y, Pontes B, Ohmstede M, *et al.* Myosin 1E localizes to actin polymerization sites in lamellipodia, affecting actin dynamics and adhesion formation. *Biol. Open* 2013, **2:** 1288-1299.

6. Iuliano, Yoshimura A, Prospéri M-T, Martin R, Knölker H-J, Coudrier E. Myosin 1b promotes axon formation by regulating actin waves propagation and growth cone dynamics. *J. Cell Biol.* 2018, **217:** 2033.

7. Joensuu M, Belevich I, Ramo O, Nevzorov I, Vihinen H, Puhka M, *et al.* ER sheet persistence is coupled to myosin 1c-regulated dynamic actin filament arrays. *Mol. Biol. Cell* 2014, **25:** 1111-1126.

8. Greenberg MJ, Lin T, Goldman YE, Shuman H, Ostap EM. Myosin IC generates power over a range of loads via a new tension-sensing mechanism. *Proc. Natl. Acad. Sci. USA* 2012, **109:** E2433-2440.

9. Laakso JM, Lewis JH, Shuman H, Ostap EM. Myosin I Can Act As a Molecular Force Sensor. *Science* 2008, **321:** 133-136.

10. Lewis JH, Lin T, Hokanson DE, Ostap EM. Temperature Dependence of Nucleotide Association and Kinetic Characterization of Myo1b. *Biochemistry* 2006, **45:** 11589-11597.

11. Guérin T, Prost J, Joanny J-F. Dynamical behavior of molecular motor assemblies in the rigid and crossbridge models. *Eur. Phys. J. E* 2011, **34:** 60.

12. Carlier MF, Pernier J, Montaville P, Shekhar S, Kuhn S, Cytoskeleton D, *et al.* Control of polarized assembly of actin filaments in cell motility. *Cell. Mol. Life Sci.* 2015, **72:** 3051-3067.

13. Veigel C, Molloy JE, Schmitz S, Kendrick-Jones J. Load-dependent kinetics of force production by smooth muscle myosin measured with optical tweezers. *Nat. Cell Biol.* 2003, **5:** 980.

14. Crevenna AH, Arciniega M, Dupont A, Mizuno N, Kowalska K, Lange OF, *et al.* Side-binding proteins modulate actin filament dynamics. *eLife* 2015, **4:** e04599.

15. Footer MJ, Kerssemakers JW, Theriot JA, Dogterom M. Direct measurement of force generation by actin filament polymerization using an optical trap. *Proc. Natl. Acad. Sci. USA* 2007, **104:** 2181-2186.

16. Komaba S, Coluccio LM. Localization of myosin 1b to actin protrusions requires phosphoinositide binding. *J. Biol. Chem.* 2010, **285:** 27686-27693.

17. Guo L, Har JY, Sankaran J, Hong Y, Kannan B, Wohland T. Molecular diffusion measurement in lipid bilayers over wide concentration ranges: a comparative study. *ChemPhysChem* 2008, **9:** 721-728.

18. Pyrpassopoulos S, Feeser EA, Mazerik JN, Tyska MJ, Ostap EM. Membrane-bound myo1c powers asymmetric motility of actin filaments. *Curr. Biol.* 2012, **22:** 1688-1692.

19. Grover R, Fischer J, Schwarz FW, Walter WJ, Schwille P, Diez S. Transport efficiency of membrane-anchored kinesin-1 motors depends on motor density and diffusivity. *Proc. Natl. Acad. Sci. USA* 2016, **113:** E7185.

20. Vogel SK, Petrasek Z, Heinemann F, Schwille P. Myosin motors fragment and compact membrane-bound actin filaments. *eLife* 2013, **2:** e00116.

21. Murrell M, Gardel ML. F-actin Buckling Coordinates Contractility and Severing in a Biomimetic Actomyosin Cortex *Proc. Natl. Acad. Sci. USA* 2012, **109:** 20820-20825

22. Kovar DR, Kuhn JR, Tichy AL, Pollard TD. The fission yeast cytokinesis formin Cdc12p is a barbed end actin filament capping protein gated by profilin. *J. Cell Biol.* 2003, **161:** 875.

23. Romero S, Le Clainche C, Didry D, Egile C, Pantaloni D, Carlier M-F. Formin Is a Processive Motor that Requires Profilin to Accelerate Actin Assembly and Associated ATP Hydrolysis. *Cell* 2004, **119:** 419-429.

24. Johnston AB, Collins A, Goode BL. High-speed depolymerization at actin filament ends jointly catalysed by Twinfilin and Srv2/CAP. *Nat. Cell Biol.* 2015, **17:** 1504.

25. Wioland H, Guichard B, Senju Y, Myram S, Lappalainen P, Jégou A, *et al.* ADF/Cofilin Accelerates Actin Dynamics by Severing Filaments and Promoting Their Depolymerization at Both Ends. *Curr. Biol.* 2017, **27:** 1956-1967.e1957.

26. Varga V, Leduc C, Bormuth V, Diez S, Howard J. Kinesin-8 Motors Act Cooperatively to Mediate Length-Dependent Microtubule Depolymerization. *Cell* 2009, **138:** 1174-1183.

27. Moores CA, Milligan RA. Lucky 13-microtubule depolymerisation by kinesin-13 motors. *J. Cell Sci.* 2006, **119:** 3905-3913.

28. Greenberg Michael J, Arpağ G, Tüzel E, Ostap EM. A Perspective on the Role of Myosins as Mechanosensors. *Biophys. J.* 2016, **110:** 2568-2576.

29. Dürre K, Keber FC, Bleicher P, Brauns F, Cyron CJ, Faix J, *et al.* Capping protein-controlled actin polymerization shapes lipid membranes. *Nat. Commun.* 2018, **9:** 1630.

30. Ennomani H, Letort G, Guérin C, Martiel J-L, Cao W, Nédélec F, *et al.* Architecture and Connectivity Govern Actin Network Contractility. *Curr. Biol.* 2016, **26:** 616-626.

31. Freeman SA, Jaumouillé V, Choi K, Hsu BE, Wong HS, Abraham L, *et al.* Toll-like receptor ligands sensitize B-cell receptor signalling by reducing actin-dependent spatial confinement of the receptor. *Nat. Commun.* 2015, **6:** 6168.

32. Noguchi T, Lenartowska M, Miller KG. Myosin VI stabilizes an actin network during Drosophila spermatid individualization. *Mol. Biol. Cell* 2006, **17:** 2559-2571.

33. Loubéry S, Delevoye C, Louvard D, Raposo G, Coudrier E. Myosin VI Regulates Actin Dynamics and Melanosome Biogenesis. *Traffic* 2012, **13:** 665-680.

34. Ciobanasu C, Faivre B, Le Clainche C. Actomyosin-dependent formation of the mechanosensitive talin–vinculin complex reinforces actin anchoring. *Nat. Commun.* 2014, **5:** 3095.

35. Pollard TD. Myosin purification and characterization. In: *Methods in Cell Biology*, vol. 24. Elsevier, 1982, pp 333-371.

36. Yamada A, Mamane A, Lee-Tin-Wah J, Di Cicco A, Prevost C, Levy D, *et al.* Catch-bond behaviour facilitates membrane tubulation by non-processive myosin 1b. *Nat. Commun.* 2014, **5:** 3624.

37. Weinberger A, Tsai F-C, Koenderink G, Schmidt T, Itri R, Meier W, *et al.* Gel-Assisted Formation of Giant Unilamellar Vesicles. *Biophys. J.* 2013, **105:** 154-164.

38. Galush WJ, Nye JA, Groves JT. Quantitative Fluorescence Microscopy Using Supported Lipid Bilayer Standards. *Biophys. J.* 2008, **95:** 2512-2519.

39. Sorre B, Callan-Jones A, Manzi J, Goud B, Prost J, Bassereau P, *et al.* Nature of curvature-coupling of amphiphysin with membranes depends on its bound density. *Proc. Natl. Acad. Sci. USA* 2012, **109:** 173-178.

40. Soumpasis DM. Theoretical analysis of fluorescence photobleaching recovery experiments. *Biophys. J.* 1983, **41:** 95-97.

41. Vilfan A, Frey E, Schwabl F. Force-velocity relations of a two-state crossbridge model for molecular motors. *Europhys. Lett.* 1999, **45**: 283-289

42. Saffman PG, Delbrück M. Brownian motion in biological membranes. *Proc. Natl. Acad. Sci. USA* 1975, **72**: 3111-3113.

Acknowledgments
We thank B. Goud for insightful discussions, C. Le Clainche (I2BC, Gif-sur-Yvette, France) for providing actin and Myosin II and critically reading the manuscript, F.-C. Tsai for SLB preparation, L. Blanchoin, C. Leduc, J. Prost, M. Henderson for carefully reading the manuscript. The authors greatly acknowledge the Cell and Tissue Imaging (PICT-IBiSA), Institut Curie, member of the French National Research Infrastructure France-BioImaging (ANR10-INBS-04). This work was supported by Institut Curie, Centre National de la Recherche Scientifique (CNRS), the European Research Council (ERC) (J.F.J., P.B. and E.C are partners of the advanced grant, project 339847 and their groups belong to the CNRS consortium CellTiss, the Labex CelTisPhyBio (ANR-11-LABX0038) and Paris Sciences et Lettres (ANR-10-IDEX-0001-02). J.P. and R.K. were funded by the ERC project 339847.

Author contributions
P.B and E.C. designed the study. J.P. and A.M. performed TIRF experiments and analyzed data; J.P. and T.L. conducted FRAP experiments; H.B. purified Myosin 1b. R.K. and J.-F.J. developed the model. P.B, E.C., J.P., R.K. and J.-F.J. wrote the paper.

Competing interests
The authors declare no competing interests.

Figure Legends

Figure 1: **Three-state crossbridge model and Myo1b-Actin gliding assays**. **(A)** Schematic representation of domain organization of Myo1b. Motor domain (blue); LCBD domain (yellow); TH1 domain (red), PH domain (cyan) that binds phosphoinositides. **(B)** Three-state crossbridge model. The motor binds to the filament with an attachment rate ω_{on}, then performs a first power-stroke of size d_1=5.1 nm. After this first power stroke the motor transits with a force-dependent (catch-bond) rate ω_{1-2} to release its stress and performs a second power-stroke d_2=3.3 nm. After this second state, the motor binds an ATP molecule and detaches from the filament with a rate ω_{det}. **(C)** Gliding assays of stabilized actin filaments (I-II) and polymerizing actin filaments (III-IV) sliding on Myo1b anchored on coverslip (I-III) or bound to a supported lipid bilayer (II-IV).

Figure 2: **Sliding on immobilized Myosin 1b increases F-actin depolymerization. (A)** Representative kymographs of stabilized F-actin (top) or polymerizing F-actin with 0.6 µM G-actin (bottom), on uncoated glass or sliding on glass coated with Myo1b (2 mM and 0.2 mM ATP (see movies S2 and S3) or MyoII (see movie S6). The sliding distance ΔX and the elongation ΔL of the filaments are indicated by white arrows. Actin fluorescence intensity is represented according to the "Fire" LUT of Image J. Scale bar, 5µm. 1 image/10 sec. **(B)** Dot plot representation of the sliding velocities v_f of stabilized (top) and polymerizing actin filaments (0.6 µM G-actin) (bottom) on immobilized Myo1b (8000 molecules/µm^2) at 2 mM (blue) or 0.2 mM (grey) ATP or sliding on MyoII at 2 mM ATP (orange). The number of analyzed filaments and the mean-values ± s.e.m. are indicated. (**C**) Filament elongation ΔL (normalized by the length of the actin subunit (su) equal to 2.7 nm) versus time for filaments shown in A (bottom) in the absence of myosins and in the presence of MyoII or Myo1b at two ATP concentrations. Polymerization rate at the barbed end v_p is deduced from the slope. **(D)** v_p as a function of G-actin concentration C_m for the different conditions. The fits correspond to $v_p = k_{on}C_m - k_{off}$, with k_{on} the rate of association of G-actin and k_{off} the rate of dissociation. C_{c+} is the critical concentration for polymerization. Inset: k_{off} for the different conditions. Error bars represent s.e.m. (n>25). **(E)** Model for the role of Myo1b motor on the dissociation (depolymerization) rate k_{off}. The filament, sliding at velocity v_f, experiences a force F_{fil} at the barbed end while the motor is attached, thus impacting k_{off}, but not the association (polymerization) rate k_{on}.

Figure 3: **Sliding on Myosin 1b bound to a supported lipid bilayer increases F-actin depolymerization (A)** Top: Diffusion coefficients of Atto488DOPE (DOPE*) and Alexa488-labelled Myo1b (Myo1b*) in a SLB with bound Myo1b, with and without 0.3 % methylcellulose (MEC), and in absence or in the presence of a dense F-actin network (n = 30). See Fig. S6 for representative FRAP experiments. Bottom: Effective diffusion coefficients of Cherry-CAAX, Cherry-Myo1b, expressed in HEK293T cells (n > 5). Error bars represent s.e.m. **(B)** Representative kymographs of non-polymerizing (top) and polymerizing F-actin (bottom) in the presence of 0.6 µM G-actin with Myo1b bound to SLBs (movie S8). Scale bar, 5µm. 1 image/10 sec. **(C)** Dot blot representation of the velocities v_f of stabilized (top) and polymerizing F-actin (bottom) sliding on immobilized Myo1b (dark blue) or on Myo1b bound to a SLB (cyan). The number of analyzed filaments is indicated. **D)** Model for filament sliding: The effective filament sliding is determined by a balance between the viscous dissipation of the motor moving with a velocity v_m in the lipid bilayer with a viscosity η_m and a filament sliding at a velocity v_f in a solution of viscosity η_b. **(E)** ΔL versus time for the single filaments shown in (B). **(F)** v_p as a function of G-actin concentration C_m for the different conditions. The fit to the data is the same as in Fig. 2D. Inset: k_{off} for the different

conditions. Error bars represent s.e.m. (n>25). **(G)** Model for force transmission: The effective force experienced by the polymerizing filament $\tilde{F_{fil}}$ is diminished by the motion in the lipid bilayer of the motor v_m at the barbed end.

Figure 1

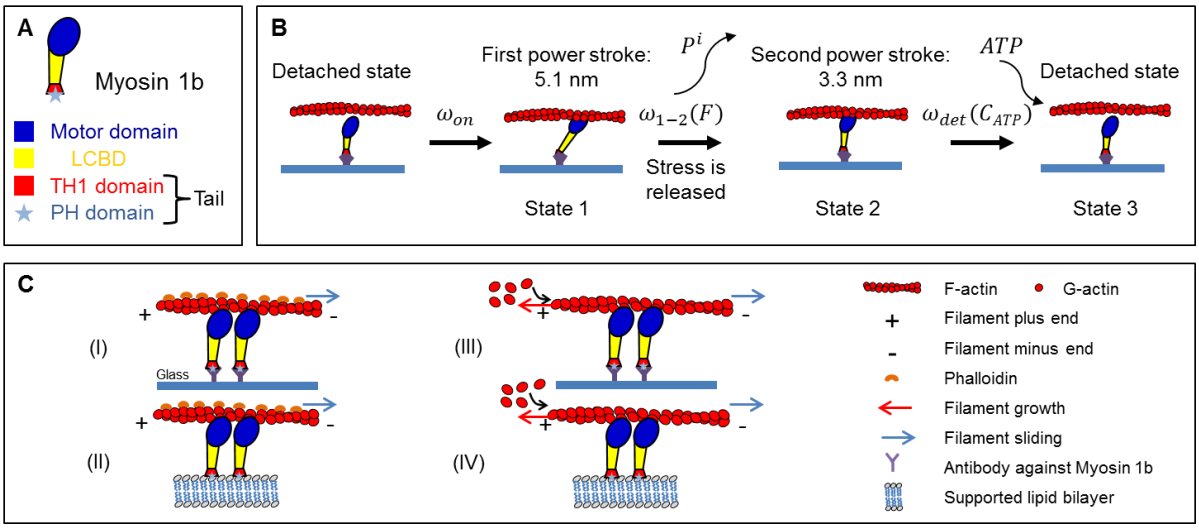
A
Myosin 1b
Motor domain
LCBD
TH1 domain
PH domain
Tail
B
Detached state
First power stroke:
5.1 nm
P^i
Second power stroke:
3.3 nm
ATP
Detached state
ω_{on}
$\omega_{1-2}(F)$
$\omega_{det}(C_{ATP})$
Stress is
released
State 1
State 2
State 3
C
(I)
(II)
(III)
(IV)
Glass
F-actin
G-actin
Filament plus end
Filament minus end
Phalloidin
Filament growth
Filament sliding
Antibody against Myosin 1b
Supported lipid bilayer

Figure 2

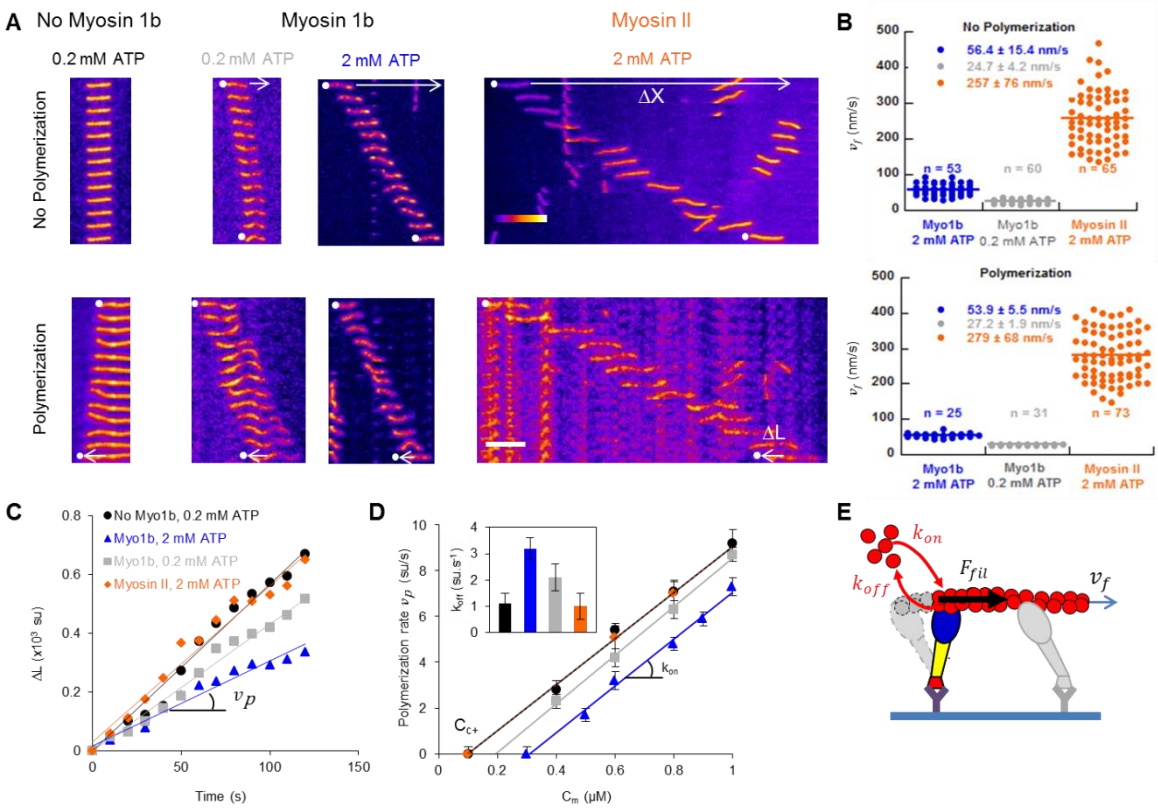
A
No Myosin 1b
Myosin 1b
Myosin II
0.2 mM ATP
0.2 mM ATP
2 mM ATP
2 mM ATP
No Polymerization
Polymerization
ΔX
ΔL
B
No Polymerization
56.4 ± 15.4 nm/s
24.7 ± 4.2 nm/s
257 ± 76 nm/s
n = 53
n = 60
n = 65
Myo1b 2 mM ATP
Myo1b 0.2 mM ATP
Myosin II 2 mM ATP
Polymerization
53.9 ± 5.5 nm/s
27.2 ± 1.9 nm/s
279 ± 68 nm/s
n = 25
n = 31
n = 73
C
No Myo1b, 0.2 mM ATP
Myo1b, 2 mM ATP
Myo1b, 0.2 mM ATP
Myosin II, 2 mM ATP
ΔL (x10³ su)
Time (s)
D
Polymerization rate (su/s)
C_m (μM)
C_c+
E
k_on
k_off
F_fil
v_f

Figure 3

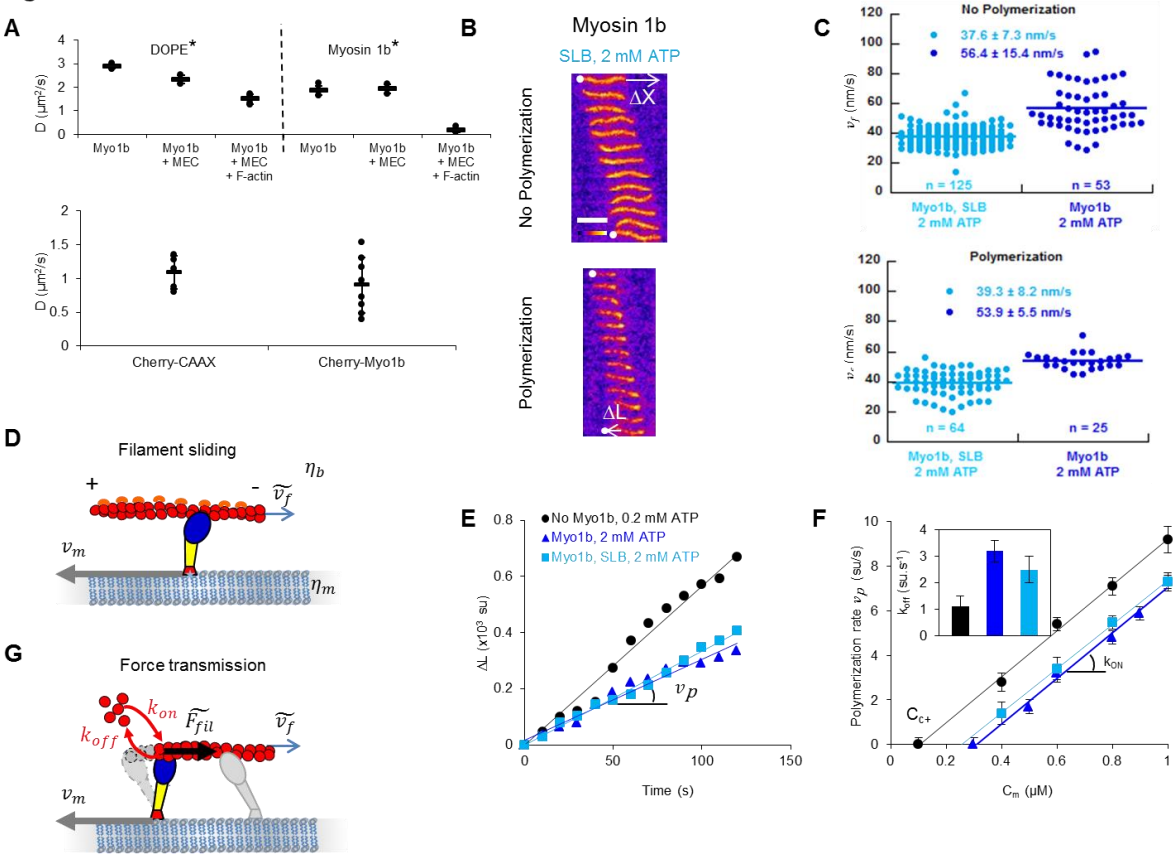

A
DOPE*
Myosin 1b*
D (μm²/s)
Myo1b
Myo1b + MEC
Myo1b + MEC + F-actin
Cherry-CAAX
Cherry-Myo1b
B
Myosin 1b
SLB, 2 mM ATP
No Polymerization
Polymerization
ΔX
ΔL
C
No Polymerization
37.6 ± 7.3 nm/s
56.4 ± 15.4 nm/s
n = 125
n = 53
Myo1b, SLB 2 mM ATP
Myo1b 2 mM ATP
Polymerization
39.3 ± 8.2 nm/s
53.9 ± 5.5 nm/s
n = 64
n = 25
D
Filament sliding
G
Force transmission
E
No Myo1b, 0.2 mM ATP
Myo1b, 2 mM ATP
Myo1b, SLB, 2 mM ATP
ΔL (x10³ su)
Time (s)
F
Polymerization rate v_p (su/s)
k_{off} (su.s⁻¹)
C_{c+}
k_{ON}
C_m (μM)

Supplementary information

Legends - Supplementary tables and figures

Table S1: Sliding velocities v_f of stabilized and polymerizing actin filaments on Myo1b or Myosin II in the different used conditions.

Table S2: Rate constants of G-actin monomer association and dissociation in the absence and presence of Myo1b or Myosin II in the different used conditions.

Figure S1: Analysis of the experimental data and calibration of the Myo1b density. (A) Left: Time-lapse images obtained by TIRF microscopy of a stabilized filament (top) (and a polymerizing filament in the presence of 1.2 µM G-actin (bottom) sliding along glass-anchored Myo1b (see movie S1). White dots indicate the filament barbed end. The white dashed represents the trajectory of the stabilized filament, and ΔX the total displacement of the filament over the period considered. L_0 and ΔL are the initial length of the polymerizing filament and its elongation, respectively. Middle: corresponding kymographs. The sliding ΔX and the elongation ΔL correspond to the white arrows. Right: Time variation of ΔX and ΔL. The sliding v_f and elongation v_p velocities are deduced from the slopes of the graphs. Actin fluorescence intensity is represented according to the "Fire" LUT of Image J. Scale bar, 5µm. 1 image/20 sec. **(B)** Myo1b density on the solid substrate or on the supported bilayer deduced from (a) the measurement of the fluorescence intensity of a reference lipid Atto488DOPE at known density in a SLB (supported lipid bilayer), and the comparison of (b) the fluorescence of Myo1b dye Alexa 488 and (c) Atto488DOPE in bulk at known concentrations (see Materials and Methods). The calibration constant A is deduced from the slope of a).

Figure S2: Impact of Myo1b on F-actin pointed end and impact of Myo1b at low density, inactivated, or in solution on the sliding and actin depolymerization at the barbed end. (A) Representative kymograph of polymerizing actin filaments, in presence of 0.6 µM G-actin, 2 mM ATP with anchored Myo1b at ≈ 8000 μm^{-2} (see movie S4). The elongation ΔL_m of the filaments at the pointed end (between the 2 dashed white lines) is indicated. Scale bar, 5 µm. 1 image/10 sec. **(B)** Representative kymographs of phalloidin stabilized filaments (top) or polymerizing actin filaments (bottom), in presence of 0.6 µM G-actin, 2 mM ATP, with Myo1b in solution (red), Myo1b without motor activity (brown), with anchored Myo1b at low density (≈500 motor/μm^2) (purple). (See movies S2, S3 and S5). Scale bar, 5µm. 1image/10 sec. **(C)** Comparison of the distribution of the velocities v_f of stabilized (top) and polymerizing F-actin (bottom) sliding on immobilized high density Myo1b, 2 mM ATP (dark blue) and 0.2 mM ATP (grey) and low density Myo1b, 2 mM ATP (purple). Velocity distributions and average velocities are indicated. Data are represented with a "Dot plot". The number of analyzed filaments is indicated. **(D)** ΔL versus time for the single filaments for the conditions shown in (A) and (B) and in the absence of Myo1b. **(E)** v_p as a function of G-actin concentration C_m for the different indicated conditions. The fit to the data is the same as in Fig. 2D. Error bars represent s.e.m. (n > 25). Inset: k_{off} for the different conditions. **(F)** Representative kymographs of depolymerizing actin filaments, in absence of G-actin (C_m= 0 µM), without Myo1b (left) or with anchored Myo1b at ≈8000 motor/μm^2 (right), with 2 mM ATP. (See movie S7). Scale bar, 5µm. 1 image/10 sec. **(G)** ΔL versus time for the single

filaments shown in (F). **(H)** v_p as a function of filament length L for single polymerizing filaments sliding along glass-anchored Myo1b in the presence of 0.6 µM G-actin and 2 mM ATP (n = 90, v_p measured during 30 sec).

Figure S3: Predictions of our model for filament sliding. (A, B) Forces exerted on the filament $F_1\rho_1$, $F_2\rho_2$ as a function for their respective age of attachment τ_1, τ_2;for (A) C_{ATP} =0.2mM and (B) C_{ATP} = 2mM. **(C, D)** Fractions of motors in state 1 (n_1) and state 2 (n_2) as a function of (C) C_{ATP}, for ω_{on}=100 s^{-1} and (D) ω_{on}, for C_{ATP}=2mM. **(E)** n_1 and n_2 as a function of C_{ATP} for ω_{on}=100 s^{-1}. The dashed line corresponds to a non-catch bond version of the motor with otherwise identical parameters (ω_{1-2}= ω_i+ω_0). **(F)** Sliding velocities of the filament v_f as a function of C_{ATP}, corresponding to the curves in (E). In all figures, we have used kinetic and mechanic parameters as described in Table I (Materials and Methods).

Figure S4: Determination of the Myo1b transition rates (ω_i, $\omega_0 \wedge \omega_{sat}$). (A) Velocity map at (A) C_{ATP}=2mM and (B) C_{ATP}=0.2mM, as a function of ω_i, ω_0 for ω_{sat}=25 s^{-1}. **(C-E)** Map of the matching error, the sum of the square difference between the sliding speeds at 0.2 and 2 mM ATP, as a function of ω_i and ω_0 (SE9) for three different values of ω_{sat}=10, 25 and 40 s^{-1}. A small matching error indicates that the sliding speeds match the measured values. Note that the red region in (B) represents the region with small squared error (error < 100$(nm/s)^2$, see (SE9)), which is never obtained for ω_{sat}=10 and 40 s^{-1}.

Figure S5: Theoretical prediction for the impact of filament sliding on depolymerization. (A) Depolymerization rate relative to that at vanishing external force k_{off}/k_{off}^0 as function of C_{ATP} for various values of the characteristic scale for the force sensitivity of the depolymerization rate of the actin f^*. **(B)** k_{off}/k_{off}^0 as function of ω_{on} at f^*=5.5 pN for the Myo1b and MyoII motor at C_{ATP}=2mM. See parameter values in Table I (Materials and Methods).

Figure S6: FRAP data of DOPE and Myo1b in a SLB. (A and B) Representative FRAP recovery curves (symbols) and the best fit with single exponential (solid line) of Atto488-DOPE (DOPE*) and Alexa488-labelled Myo1b (Myosin 1b*) in a SLB with bound Myo1b, with (in red) or without (in black) 0.3 % methylcellulose (MEC), and in absence or presence (in cyan) of a dense F-actin network.

Figure S7: Effect of bulk viscosity on relative velocity of the filament. Velocity of the filament $\widetilde{v_f}$, relative to its velocity on a solid substrate v_0 (Eq. SE14), for different values of motor density n. Increasing the bulk viscosity, relative to the membrane viscosity, induces motion of the motors in the bilayer, hence decreasing the effective velocity of the filament. Increasing the density of molecular motors on the surface increases the effective membrane friction and hence increases the sliding speed.

Figure S8: Myo1b bound to giant liposomes produces membrane invagination in presence of stabilized actin filaments. Representative confocal microscopy images of tubules induced by Myo1b bound to a PI(4,5)P_2-containing GUV in the presence of stabilized actin filaments. We have observed tubulation in the equatorial plane for 16 GUVs over a total of 96. Labeling corresponds to **(A)** 0.3% Texas Red DHPE (mol/mol) and **(B)** stabilized actin filaments with Alexa Fluor 647 phalloidin. Scale bars, 5 µm.

Legends - Movies

Movie S1: Stabilized and polymerizing actin filaments sliding along glass-anchored Myo1b (corresponding to Fig. S1A).
Sliding of stabilized filaments labeled with phalloidin-Alexa547 (a) and polymerizing filaments (b) with 1.2 µM actin in bulk (10 % Alexa594 labeled), along Myo1b (8000 μm^{-2}) at 2 mM ATP. White arrow indicates the initial position of the filament corresponding to the kymograph in Fig. S1A. Note that no filament breaking is observed during these experiments. Scale bar 5 µm. Time in s.

Movie S2: Effect of the ATP concentration and Myo1b density on stabilized actin filaments sliding along glass-anchored Myo1b (corresponding to Figs. 2A and S2B).
Filaments stabilized with phalloidin-Alexa547 as a function of ATP concentration (0.2 and 2 mM ATP), without Myo1b (a), sliding on Myo1b at high density (8000 μm^{-2}) (b, c) or at low density (400 μm^{-2}) (d). Wide field movies followed by single filament movies corresponding to kymographs shown in Fig. 2A-Top panel and Fig. S2B-Top panel. White arrows indicate the initial position of single filaments. Scale bar 5 µm. Time in s.

Movie S3: Effect of ATP concentration and Myo1b density on polymerizing actin filaments sliding along glass-anchored Myo1b (corresponding to Fig. S2A).
Polymerizing filaments as a function of ATP concentration as a function of ATP concentration (0.2 and 2 mM ATP), without Myo1b (a), sliding on Myo1b at high density (8000 μm^{-2}) (b, c) or at low density (400 μm^{-2}) (d). Wide field movies followed by single filament movies corresponding to kymographs shown in Fig. 2A-Bottom panel and Fig. S2B-Bottom panel. White arrows indicate the initial position of single filaments. Scale bar 5 µm. Time in s.

Movie S4: No effect at pointed-end on polymerizing actin filaments sliding along glass-anchored Myo1b.
Polymerizing actin filaments with 0.6 µM actin (10 % Alexa594 labeled), along Myo1b (8000 μm^{-2}) at 2 mM ATP. The white arrow indicates the initial position of the filament shown in Fig. S2A. Scale bar 5 µm. Time in s.

Movie S5: Stabilized and polymerizing actin filaments with Myo1b in bulk or inactivated (corresponding to Fig. S2B).
Filaments stabilized with phalloidin-Alexa547 and polymerizing actin filament, with 0.6 µM actin (10 % Alexa594 labeled), 2 mM ATP, 300 nM Myo1b in the bulk, or bound but inactivated. Note that in the bottom left movie, one filament seems to move but it suddenly appears in the field of view while sedimenting. Frames correspond to the kymographs shown in Fig. S2B; arrows indicate the initial position of these filaments. Scale bar 5 µm. Time in s.

Movie S6: Stabilized and polymerizing actin filaments sliding along glass-anchored MyoII (corresponding to Fig. 2A).
Filaments stabilized with phalloidin-Alexa547 or polymerizing at 0.6 µM actin (10 % Alexa594 labeled), sliding along MyoII at 2 mM ATP. Frames correspond to the kymographs

shown in Fig. 2A; arrows indicate the initial position of these filaments. Scale bar 5 µm. Time in s.

Movie S7: Impact of Myo1b on the depolymerization of actin filaments in the absence of G-actin in the bulk (corresponding to Fig. S2F).
Filaments depolymerizing in the absence of G-actin in bulk, without Myo1b, or sliding along Myo1b, at 2 mM ATP. Frames correspond to the kymographs shown in Fig. S2F; arrows indicate the initial position of these filaments. Scale bar 5 µm. Time in s.

Movie S8: Stabilized and polymerizing actin filaments sliding along Myo1b bound to SLBs (corresponding to Fig. 3B).
Sliding of filaments stabilized with phalloidin-Alexa547 or polymerizing at 0.6 µM actin (10 % Alexa594 labeled), along Myo1b bound to SLBs (≈ 8500 μm^{-2}) at 2 mM ATP. Wide field movies followed by single filament movies corresponding to kymographs shown in Fig. 3B. White arrows indicate the initial position of single filaments. Scale bar 5 µm. Time in s.

Table S1

	Myosin	[ATP] (mM)	Density (molecules/μm^2)	Condition	Velocity (nm/s)
On glass	Myosin 1b	2	8393 ± 430	No polymerization	56.4 ± 15.4
		2	8444 ± 873	Polymerization	53.9 ± 5.5
		0.2	8776 ± 1293	No polymerization	24.7 ± 4.2
		0.2	8876 ± 459	Polymerization	27.2 ± 1.9
		2	447 ± 20	No polymerization	33.3 ± 3.1
		2	533 ± 84	Polymerization	35.6 ± 6.2
	Myosin II	2	Not reported	No polymerization	257 ± 76
		2	Not reported	Polymerization	279 ± 68
On SLB	Myosin 1b	2	8770 ± 170	No polymerization	37.6 ± 7.3
		2	8657 ± 1251	Polymerization	39.3 ± 8.2

Table S2

	Myosin	[ATP] (mM)	Density (molecules/μm^2)	k_{on} ($su.\mu M^{-1}.s^{-1}$)	k_{off} ($su.s^{-1}$)	Critical concentration C_{c+} (μM)
In solution	No Myosin	0.2		10.3 ± 0.8	1.1 ± 0.4	0.10 ± 0.05
	No Myosin	2		10.9 ± 0.6	1.4 ± 0.4	0.13 ± 0.06
	Myosin 1b	2	Not reported	11.4 ± 1.1	1.8 ± 0.5	0.16 ± 0.04
On glass	Myosin 1b	2	8444 ± 873	10.3 ± 0.5	3.2 ± 0.4	0.31 ± 0.05
		0.2	8876 ± 459	10.7 ± 0.9	2.1 ± 0.5	0.20 ± 0.04
		2	533 ± 84	10.0 ± 1.2	2.6 ± 0.6	0.26 ± 0.08
	No motor	2	7767 ± 423	10.9 ± 0.8	1.6 ± 0.5	0.15 ± 0.05
	Myosin II	2	Not reported	10.0 ± 0.8	1.0 ± 0.5	0.10 ± 0.05
On SLB	Myosin 1b	2	8657 ± 1251	9.9 ± 0.8	2.5 ± 0.5	0.26 ± 0.05

Figure S1

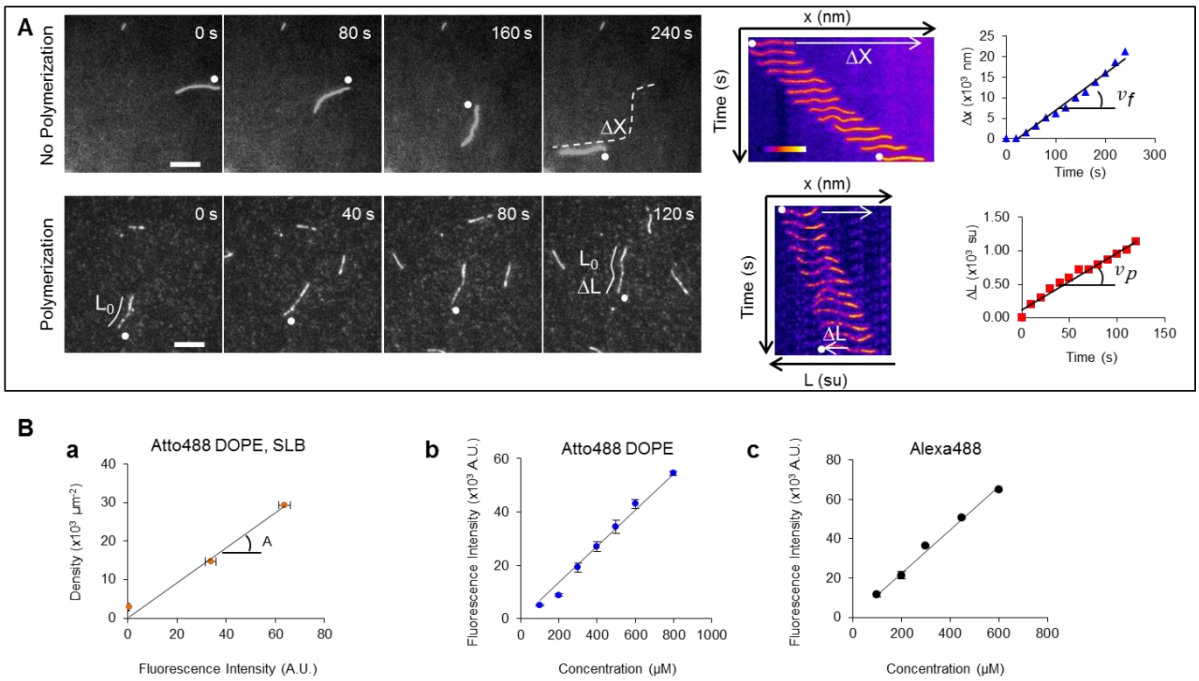
A
No Polymerization
0 s
80 s
160 s
240 s
ΔX
x (nm)
Time (s)
Δx (x10³ nm)
Time (s)
Polymerization
0 s
40 s
80 s
120 s
L0
ΔL
L (su)
ΔL (x10³ su)

B
a
Atto488 DOPE, SLB
Density (x10³ µm⁻²)
Fluorescence Intensity (A.U.)
b
Atto488 DOPE
Fluorescence Intensity (x10³ A.U.)
Concentration (µM)
c
Alexa488
Fluorescence Intensity (x10³ A.U.)
Concentration (µM)

Figure S2

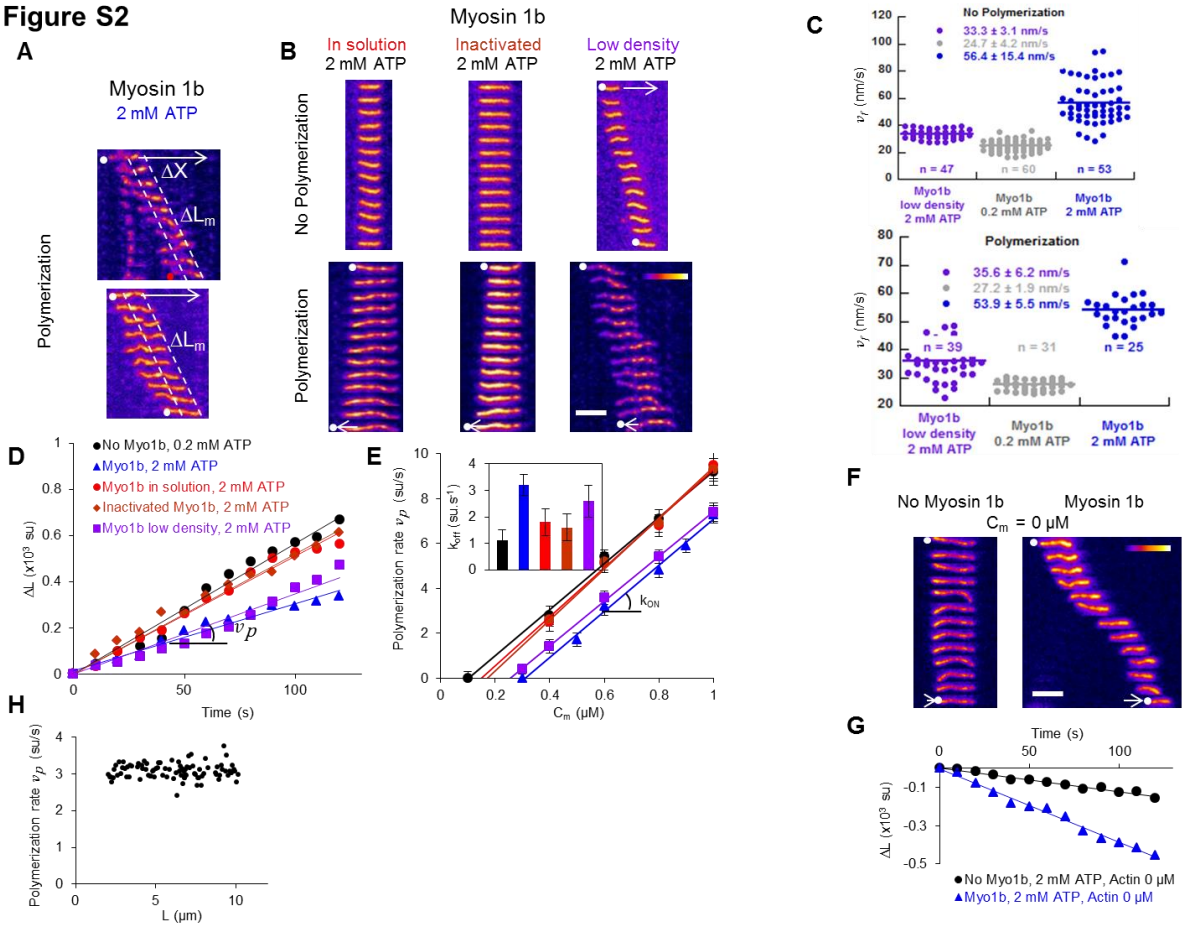
A
Myosin 1b
2 mM ATP
ΔX
ΔLm
Polymerization
B
Myosin 1b
In solution
2 mM ATP
Inactivated
2 mM ATP
Low density
2 mM ATP
No Polymerization
Polymerization
C
No Polymerization
33.3 ± 3.1 nm/s
24.7 ± 4.2 nm/s
56.4 ± 15.4 nm/s
n = 47
n = 60
n = 53
Myo1b low density 2 mM ATP
Myo1b 0.2 mM ATP
Myo1b 2 mM ATP
Polymerization
35.6 ± 6.2 nm/s
27.2 ± 1.9 nm/s
53.9 ± 5.5 nm/s
n = 39
n = 31
n = 25
D
No Myo1b, 0.2 mM ATP
Myo1b, 2 mM ATP
Myo1b in solution, 2 mM ATP
Inactivated Myo1b, 2 mM ATP
Myo1b low density, 2 mM ATP
ΔL (x10³ su)
Time (s)
E
Polymerization rate vp (su/s)
koff (su.s⁻¹)
kON
Cm (μM)
F
No Myosin 1b
Myosin 1b
Cm = 0 μM
G
Time (s)
ΔL (x10³ su)
No Myo1b, 2 mM ATP, Actin 0 μM
Myo1b, 2 mM ATP, Actin 0 μM
H
Polymerization rate vp (su/s)
L (μm)

Figure S3

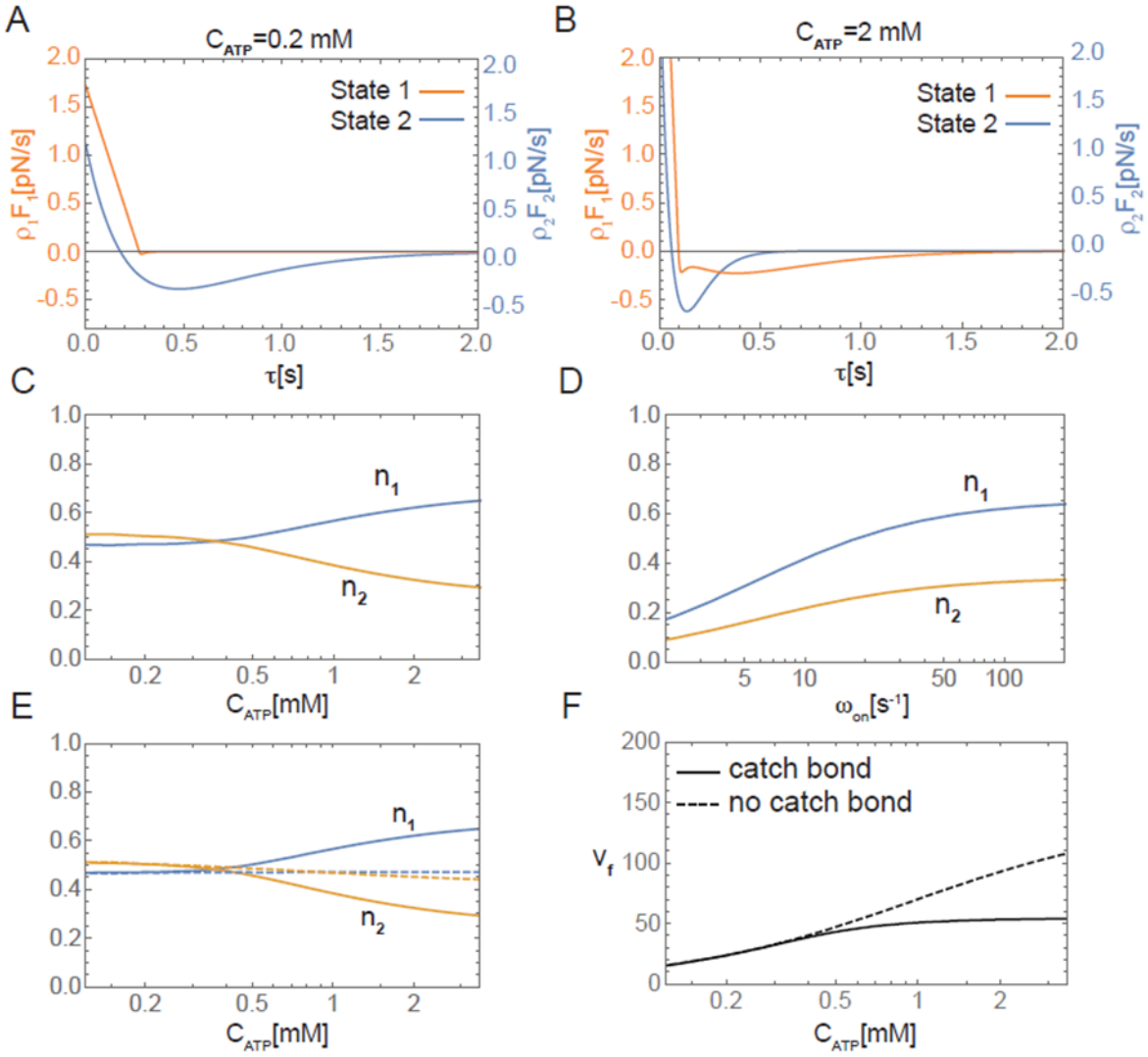
A
C_ATP=0.2 mM
State 1
State 2
ρ1F1[pN/s]
ρ2F2[pN/s]
τ[s]
B
C_ATP=2 mM
State 1
State 2
ρ1F1[pN/s]
ρ2F2[pN/s]
τ[s]
C
n1
n2
C_ATP[mM]
D
n1
n2
ω_on[s^-1]
E
n1
n2
C_ATP[mM]
F
catch bond
no catch bond
V_f
C_ATP[mM]

Figure S4

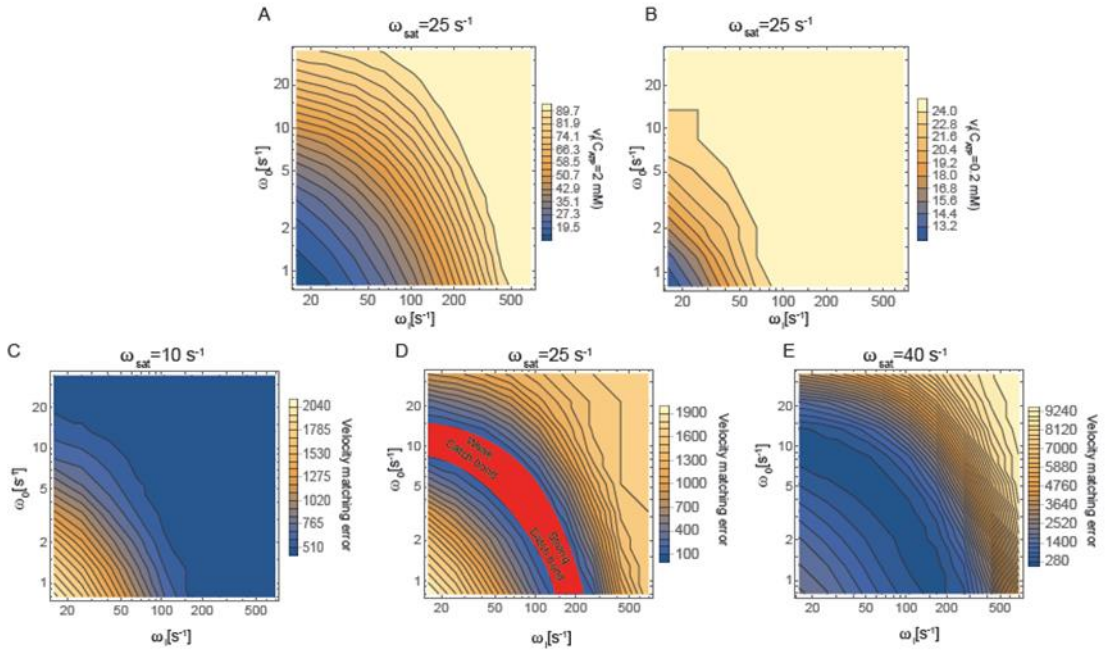
A
ω_sat=25 s^-1
B
ω_sat=25 s^-1
C
ω_sat=10 s^-1
D
ω_sat=25 s^-1
E
ω_sat=40 s^-1
ω_0[s^-1]
ω_i[s^-1]
v_i(C_AP=2 mM)
v_i(C_AP=0.2 mM)
Velocity matching error
Wave Catch bond
Ground Catch bond

Figure S5

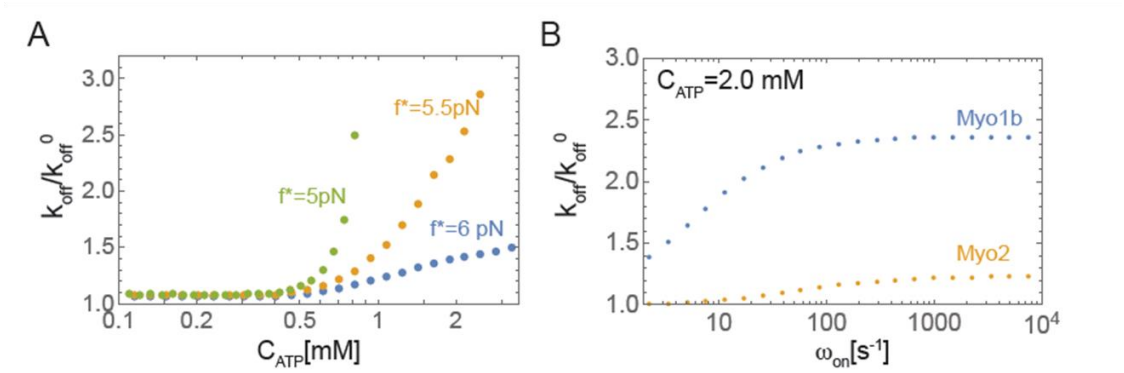
A
B
3.0
2.5
2.0
1.5
1.0
k_{off}/k_{off}^0
f*=5.5pN
f*=5pN
f*=6 pN
0.1
0.2
0.5
1
2
C_{ATP}[mM]
C_{ATP}=2.0 mM
Myo1b
Myo2
10
100
1000
10^4
$\omega_{on}[s^{-1}]$

Figure S6

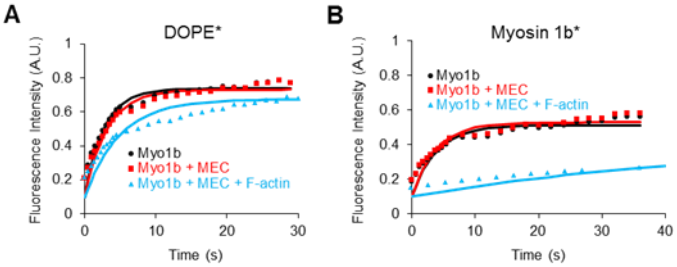
A
DOPE*
Fluorescence Intensity (A.U.)
Time (s)
Myo1b
Myo1b + MEC
Myo1b + MEC + F-actin
B
Myosin 1b*
Fluorescence Intensity (A.U.)
Time (s)
Myo1b
Myo1b + MEC
Myo1b + MEC + F-actin

Figure S7

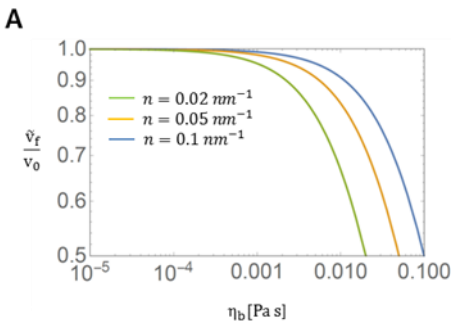
A
1.0
0.9
0.8
0.7
0.6
0.5
$\frac{\tilde{v}_f}{v_0}$
$n = 0.02\ nm^{-1}$
$n = 0.05\ nm^{-1}$
$n = 0.1\ nm^{-1}$
10^{-5}
10^{-4}
0.001
0.010
0.100
η_b [Pa s]
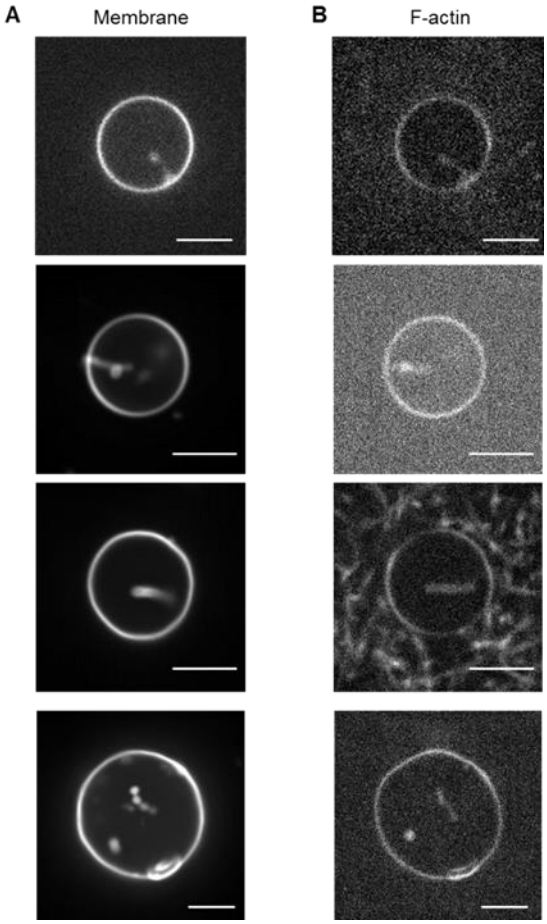
Figure S8